# Numerical study of on-board fuel reforming in a catalytic plate reactor for solid-oxide fuel cells

Vinod M. Janardhanan[a,1], Srinivas Appari[a], Sreenivas Jayanti[a], Olaf Deutschmann[b]

[a]*Indian Institute of Technology, Hyderabad, Yeddumailaram 502 205, India*
[b]*Karlsruhe Institute of Technology, Engesserstr.20, D-76131 Karlsruhe, Germany*

## Abstract

A pseudo transient numerical model is used for the simulation of a multi-functional catalytic plate reactor (CPR). The work mainly addresses the problems associated with on-board reforming for solid oxide fuel cells. Heat management is achieved by indirectly coupling partial oxidation with reforming. Water management is achieved by partially recycling the anode stream from a solid-oxide fuel cell. The model uses detailed heterogeneous chemistry for reforming and oxidation reactions occurring on the catalyst beds.

*Key words:*
Auxiliary Power Units, Catalysis, Catalytic plates reactors, Reforming, Partial oxidation

## 1. Introduction

Natural gas is widely used for transportation and worldwide there are 11.2 million vehicles running on natural gas (IANGV, 2010). In this paper we address the on-board reforming of natural gas for SOFC, however, except the reaction kinetics the modeling framework will remain the same for other transport fuels as well. Steam reforming can turn out to be counter productive due to added system complexity associated with on-board water management and the need for an additional reactant stream (Lindermeir et al., 2007). However, once the fuel cell is in operation auto-thermal reforming can be achieved by recycling the anode stream.

Steam reforming of natural gas is an important chemical process for the production of syngas ($H_2$ and CO) (Schädel et al., 2009, Bharadwaj and Schmidt, 1995), which is an ideal fuel for SOFC. Another important chemical route for the conversion of hydrocarbons to syngas is partial oxidation. Since $CH_4$ is the major constituent of natural gas we consider $CH_4$ as the fuel in this study.

There are many studies concerning the reforming and oxidation of $CH_4$ to syngas (Clarke et al., 1997, Schwiedernoch et al., 2003, Xu and Froment, 1989a, Bharadwaj and Schmidt, 1995). Higher selectivity and better heat and mass transfer rates can be achieved if reforming or oxidation is carried out in micro-structured reactors (Kolb and Hessel, 2004, Kiwi-Minsker and Renken, 2005). The enhanced heat transfer rate in micro-structured reactors can be exploited in catalytic plate reactors (CPR), where exothermic reactions are combined with endothermic reactions in a single reactor designed like a heat exchanger (Vlachos and Caratzoulas, 2010). In this set up the exothermic and endothermic reactions are separated by a thin wall as shown in Fig. 1. The system may or may not have porous catalyst coating (Kolb and Hessel, 2004) and different catalysts may be applied on either side of the wall depending on the nature of reactions desired (Vlachos and Caratzoulas, 2010). For example Ni or Rh can be a good catalyst for reforming on the other hand Pt can be used for oxidation. In CPR the coupling of endothermic and exothermic reactions are accomplished by means of indirect heat transfer.

There are many studies on the modeling of CPR for various applications. Zanfir and Gavriilidis carried out parametric studies related to channel height and catalyst layer thickness by coupling $CH_4$ reforming and $CH_4$ oxidation in a CPR. Their model equations resolved the flow channels and the solid wall two dimensionally and the catalyst bed one dimensionally under steady state conditions (Zanfir and Gavriilidis, 2003). Keeping the bed thickness to flow velocity ratio constant, they found that increasing bed thickness resulted in lower conversions. Using the same mathematical model they also analyzed the influence of counter current and co-current arrangement of CPR for steam reforming of methane. They used the global reforming kinetics of $CH_4$ on Ni reported by Xu and Froment (Xu and Froment, 1989b) in the reforming channel, whereas a first order kinetics is used to represent the catalytic combustion of $CH_4$ in the oxidation channel (Zanfir and Gavriilidis, 2004). Based on this study they concluded that co-flow configuration can avoid hot spots which are observed in the counter flow configuration. Nevertheless, they found the conversion to be higher for counter flow configuration.

In another study Baldea and Daoutidis carried out transient analysis of CPR (Baldea and Daoutidis, 2007). Similar to

---

Zanfir and Gavriilidis they also used global kinetic formulation for CH$_4$ reforming reported by Xu and Froment (Xu and Froment, 1989b). For oxidation they have considered water-gas shift reaction and the kinetic expressions are again taken from Xu and Froment (Xu and Froment, 1989b). They found that certain conditions such as increasing the flow velocity resulted in reactor extinction. There are several other reported studies that utilize CPR. For instance Kim et al., proposed a mathematical model for integrated reaction and heat exchanger model for micro-reactor based water-gas shift process. They carried out a parametric study on the CO conversion (Kim et al., 2005). Deshmukh and Vlachos modeled propane combustion and ammonia oxidation in a CPR using CFD (Deshmukh and Vlachos, 2005). Stefanidis et al., studied the coupling of CH$_4$ steam reforming with propane combustion in a CPR using a pseudo 2D model (Stefanidis et al., 2009, Stefanidis and Vlachos, 2008).

The present work numerically studies the feasibility of on-board fuel processing by combining partial oxidation and steam reforming in a catalytic plate reactor. The work differs from the above reported ones in various aspects. All the above reported work implements global reaction kinetics for reforming and oxidation, whereas in this work we implement detailed kinetic models for the surface reactions. The porous media transport is implemented using Dusty Gas Model (DGM). The DGM accurately captures molecular diffusion acting in series with Knudsen diffusion which is typical in micro-structured pore networks and the total species flux evaluated also accounts for pressure driven diffusion. The pure component properties are evaluated from standard kinetic theory expressions. The study is carried out from the perspective of using CPR as an on-board reformer for SOFC-APU by recycling the anode stream. From the application perspective the present study is quite distinct from the above mentioned reports.

## 2. Numerical model

The numerical model presented here treats coupled interactions of mass and heat transport with detailed kinetic schemes for chemical reactions occurring on the catalyst surface.

### *Channel flow*

The flow of gas mixture through the top and bottom channels is modeled as plug flow according to(Zhu et al., 2005)

$$\frac{d(\rho u Y_k)}{dz} = \frac{4}{D_{\text{h}}} J_k W_k \quad k = 1, \ldots, K_{\text{g}}. \tag{1}$$

Here $J_k$ is the molar flux of species $k$ at the interface between flow channel and the porous catalyst bed. Since the channel dimensions we consider here are quite small ($\sim$1mm), the plug flow assumption is adequate to represent the species transport

in the channels. Summing Eq. 1 over all chemical species $K_{\text{g}}$ leads to the total continuity equation as

$$\frac{d(\rho u)}{dz} = \sum_{k=1}^{K_{\text{g}}} \frac{4}{D_{\text{h}}} J_k W_k. \tag{2}$$

The local density in the flow channel is calculated from the ideal gas equation as

$$\rho = \frac{p \bar{W}}{RT}, \tag{3}$$

with $\bar{W}$ defined as

$$\bar{W} = \sum_{k=1}^{K_{\text{g}}} X_k W_k \tag{4}$$

The energy balance equation for the flow channels is written as

$$\rho u c_p \frac{dT}{dz} = \frac{4}{D_{\text{h}}} h(T_{\text{s}} - T) + \frac{4}{D_{\text{h}}} \sum_{k=1}^{K_{\text{g}}} J_k W_k h_k \tag{5}$$

The heat transfer coefficient $h$ in the flow channels is defined as

$$h = \frac{\text{Nu} \lambda_{\text{f}}}{D_{\text{h}}} \tag{6}$$

The Nusselt number Nu is defined according to (Hayes and Kolaczkowski, 1997)

$$\text{Nu} = 3.095 + 8.933 \left( \frac{1000}{\text{Gz}} \right)^{-0.5386} \exp \left( - \frac{6.7275}{\text{Gz}} \right), \tag{7}$$

where $Gz$ is the Graetz number defined as

$$\text{Gz} = \frac{D_{\text{h}}}{z} \text{RePr} \tag{8}$$

### *Porous media flow*

The flow through porous bed is modeled as one dimensional, but transverse to the direction of flow through the channels as

$$\frac{dJ_k}{dy} = A_{\text{s}} \dot{s}_k \quad k = 1, \ldots, K_{\text{g}}. \tag{9}$$

The species molar flux $J_k$ in the porous bed is evaluated using DGM equation as (Zhu et al., 2005)

$$J_k = - \sum_{l=1}^{K_{\text{g}}} \mathcal{D}_{kl}^{\text{DGM}} \nabla [X_l] - \left( \sum_{l=1}^{K_{\text{g}}} \mathcal{D}_{kl}^{\text{DGM}} \frac{[X_l]}{\mathcal{D}_{l,\text{Kn}}^{\text{e}}} \right) \frac{B_{\text{g}}}{\mu} \nabla p \tag{10}$$

The DGM diffusion coefficients $\mathcal{D}_{kl}^{\text{DGM}}$ can be represented as a matrix inverse

$$\mathcal{D}_{kl}^{\text{DGM}} = \mathcal{H}^{-1}, \tag{11}$$

where the elements of the $\mathcal{H}$ matrix are

$$h_{kl} = \left[ \frac{1}{\mathcal{D}_{k,\text{Kn}}^{\text{e}}} + \sum_{j \neq k} \frac{X_l}{\mathcal{D}_{kj}^{\text{e}}} \right] \delta_{kl} + (\delta_{kl} - 1) \frac{X_k}{\mathcal{D}_{kl}^{\text{e}}} \tag{12}$$

The Knudsen diffusion coefficient $\mathcal{D}_{l,\text{Kn}}^{\text{e}}$ in the above equation is defined as

$$\mathcal{D}_{l,\text{Kn}}^{\text{e}} = \frac{\epsilon}{\tau} \frac{d_p}{3} \sqrt{\frac{8RT}{\pi W_k}}. \tag{13}$$

## Solid phase heat balance

Since the time scale of heat transport in the solid media is larger compared to mass transport and chemical kinetics transient equations are used for the heat balance. Moreover, the thickness of parallel plate reactor is much smaller compared to its length, therefore, any variation in temperature along the thickness is neglected and hence modeled as 1D according to

$$\rho_s c_{p_s} \frac{\partial T_s}{\partial t} = \frac{\partial}{\partial z}\left(\lambda \frac{\partial T_s}{\partial z}\right) - \frac{4}{D_h} h(T_s - T) \quad (14)$$

The first and second term on the right hand side of Eq. 14 respectively represents the axial conduction in the parallel plate and the heat lost to the gas-phase.

The equation systems are solved using a pseudo transient approach. A time integration is carried out for the solid phase heat balance. For each time step equations 1, 2, 3  5 and  9 forms a system of differential algebraic equations, which are solved after discretization using the DAE solver LIMEX (Deuflhardt et al., 1987).

## Boundary conditions

The inlet boundary conditions at time $t=0$ are given in Table 1. At the reactor exit the following Neumann boundary conditions are used:

$$\left.\frac{\partial T}{\partial z}\right|_{z=L} = 0, \qquad \left.\frac{du}{dz}\right|_{z=L} = 0, \qquad \left.\frac{dY_k}{dz}\right|_{z=L} = 0. \quad (15)$$

At the interface between the wall and the porous bed zero flux boundary condition is imposed for species transport, i.e

$$J_k = 0 \quad k = 1, \ldots, K_g. \quad (16)$$

## Elementary kinetics

A modified Arrhenius expression is used for the calculation of reaction rate constant based on mean field approximation according to

$$k_{fi} = A_i \left(\frac{T}{T^0}\right)^{\beta_i} \exp\left(-\frac{E_{ai}}{RT}\right) \prod_{k=K_g+1}^{K_g+K_s} \theta_k^{\mu_{ki}} \exp\left(-\frac{\epsilon_{ki}\theta_k}{RT}\right) \quad (17)$$

Here, $k_{fi}$ is the rate constant for the $i$th reaction, $\mu_{ki}$ and $\epsilon_{ki}$ are the parameters modeling the surface coverage dependency of rate constant for $i$th reaction and $\theta_k$ is the surface coverage of the $k$th chemical species. The site coverages of surface species $\theta_k$ can be obtained by solving the following equation:

$$\frac{d\theta_k}{dt} = \frac{\dot{s}_k}{\Gamma}, \quad k = K_g + 1, \ldots K_g + K_s, \quad (18)$$

where $\Gamma$ is the available site density. At steady state the above equation becomes

$$\dot{s}_k = 0, \quad k = K_g + 1, \ldots K_g + K_s, \quad (19)$$

for surface adsorbed species indicating that the surface composition is invariant in time (although varying spatially). More details about surface chemistry implementation are published elsewhere (Janardhanan et al., 2007).

## 3. Results and discussions

On-board reforming generally leads to added system complexity since $H_2O$ and/or $CO_2$ needs to be handled separately. Additionally since reforming reaction is endothermic it also demands for energy input. Therefore, for practical applications auto-thermal reforming is carried out by recycling the anode stream. In this work we address the problems of heat and $H_2O/CO_2$ management by using a CPR which couples exothermic oxidation of $CH_4$ with steam/dry reforming. Although we are considering $CH_4$ (major constituent of natural gas) in this study, the modeling framework remains the same for any transportation fuel. Another advantage of using micro-scale reactors for this application is that tight coupling of cell stack and the reformer can be achieved.

A schematic representation of the CPR is shown in Fig. 1. In such a set up the heat demand for steam reforming is met by the heat liberated from the oxidation reactions. The gas phase fuel compositions at channel inlets and the geometrical parameters for the reactor are listed in Table 1. The elementary step surface reaction mechanism considered for $CH_4$ reforming on Ni consists of 42 reactions among 6 gas-phase species and 12 surface adsorbed species (Janardhanan and Deutschmann, 2006). The surface reaction mechanism used for the partial oxidation of $CH_4$ on Rh consists of 38 reactions among 6 gas-phase species and 11 surface adsorbed species (Schwiedernoch et al., 2003). Gas phase reactions are neglected due to the low temperatures considered here. The rationale for choosing Rh for partial oxidation is that in comparison to Ni, Rh based catalysts display both high activity and stability during the partial oxidation of $CH_4$ to synthesis gas (de Smet, 2000).

For recycling study we consider 30% $CH_4$ and 70% air entering the oxidation channel at 923.15 K and 40 cm s$^{-1}$. Assuming that the products from the oxidation and reforming channels are fully converted to $H_2O$ and $CO_2$ in a SOFC (i.e 100% fuel utilization) the molar flow rate of $CH_4$ stream at the reformer channel inlet is set according to

$$\dot{n}_{CH_4} = \frac{\dot{n}_{H_2O}}{3} \quad (20)$$

Here R is the recycle ratio and $\dot{n}_{H_2O}$ is the molar flow rate of $H_2O$ in the anode stream from SOFC. In SOFC there is mass addition into the anode chamber which is equal to the mass loss in the cathode chamber. However, we neglect any mass added into the anode chamber in calculating the molar flow rate of $H_2O$ at the anode exit.

The exit compositions from the oxidation channel are displayed in Fig. 2. The major products from the oxidation channel are $H_2$, CO and $H_2O$. $CH_4$ conversion reaches steady state after 80 seconds and $H_2O$ composition decreases as time progresses. Pure air is considered to enter the reforming channel at time $t=0$ and the inlet compositions begin to change as products start forming at the oxidation channel exit. Figure 3 displays the inlet compositions at the reforming channel inlet as a function of time. 20% of the anode stream is recycled to

the reforming channel with additional $CH_4$ stream according to Eq. 20. Since the anode exhaust consists only $H_2O$, $CO_2$, and unreacted $N_2$, the reforming channel inlet consists of $CH_4$ in addition to the species in the anode exhaust. Eq. 20 maintains a S/C ratio of 3 at the reforming channel inlet.

Assuming that $CH_4$ is stored on-board at 300 K, and the fuel cell exhaust stream temperature is 1050 K, 20% of the anode recycle is enough to bring the temperature of the mixture at the reforming channel inlet to 792 K. This is calculated according to the following enthalpy balance

$$\dot{m}_{ref}h_{ref}(T) = \dot{m}_{anode}h_{anode}(1050K) + \dot{m}_{CH_4}h_{CH_4}(300K). \quad (21)$$

In the above equation the enthalpies are calculated using JANAF polynomials and is solved using Newton iteration. Sensible heat available with the rest of 80% anode stream and the cathode exhaust ($O_2$ depleted air) can be heat exchanged to bring the temperature of the fuels to 923 K at the reactor inlet. With 20% anode recycle the reforming channel inlet velocity at steady state is ~22 cm/s.

The exit compositions from the reforming channel are shown in Fig. 4. Similar to the oxidation channel exit, steady state is achieved in ~80 seconds. For the case considered here the exit temperature of the stream is shown in Fig. 5. An optimal condition would be a C/O ratio in the oxidation channel which meets the energy requirement of the reforming reactions in the reforming channel. However, due to the limitations posed by the oxidation mechanism (the elementary kinetics model that we use for partial oxidation of $CH_4$ on Rh is valid only for C/O ratios above 1.7) we do not strive to seek the optimum conditions. Moreover, the optimum conditions can vary from case to case since they are also depended on other parameters such as inlet flow rates, inlet temperatures, specific area etc.

The species profiles within the oxidation channel at steady state are shown in Fig. 6. $O_2$ in the oxidation channel is fully converted within few millimeters from the reactor inlet. Once $O_2$ is fully converted the $H_2O$ which is formed in the oxidation phase further converts $CH_4$ downstream the reactor. $CH_4$ mole fractions at the exit of the reactor is about 3.5%. Similarly the species profiles for the reforming channel at steady state are shown in Fig. 7. Unlike the oxidation channel the species profiles does not reach steady state within the reforming channel. However, the bed thickness can be increased in-order to achieve complete conversion of $CH_4$ within the reactor.

For parameter study we fix the inlet compositions at the reforming channel as 13.6% $CH_4$, 40.8% $H_2O$, 20.4% $CO_2$ and 25.2% $N_2$ entering at a velocity of 0.2 m s$^{-1}$ and 923.15 K. The oxidation channel inlet composition is given in Table 1. The inlet velocity and bed thickness at the oxidation side are maintained respectively at 40 cm s$^{-1}$ and 50 μm.

The conversion in the reforming channel and the channel exit temperature as a function of specific catalyst area is shown in Fig. 8. As expected the conversions increase with increasing specific area. Specific area of the Rh bed is kept constant at $35 \times 10^4$ m$^{-1}$ and that of Ni bed is varied from $5 \times 10^4$ to $150 \times 10^4$ m$^{-1}$. The conversion reaches the maximum possible value asymptotically. Significant increase in conversion is achieved at lower values. Increasing specific area beyond $100 \times 10^4$ m$^{-1}$ does not affect the conversion significantly. Increasing the specific area of the reforming bed also brings down the exit temperature. The temperature drops because of the higher extent of reforming achieved due to increased specific area.

The conversion as a function of bed thickness on the reforming side is displayed in Fig. 9. The thickness of Rh bed is kept constant at 50 μm and the Ni bed thickness is varied from 10 to 100 μm. Similar to specific area, $CH_4$ conversion also increases with increasing bed thickness. From the trend it is obvious that the conversion will level off asymptotically with bed thickness.

The selectivity for $H_2$ in the reforming channel as well as in the oxidation channel is shown in Fig. 10. As expected the selectivity increases with increasing specific area on the reforming side, whereas it decreases slightly on the oxidation side. Figure. 11 shows the $CH_4$ conversion in the oxidation channel as a function of specific area on the reforming side. As the specific area increases, more $CH_4$ is converted on the reforming side. However, the temperature drops due to the higher extent of reforming and as a result $CH_4$ conversion drops on the oxidation side. Since the conversion drops the $H_2$ selectivity also decreases correspondingly. The CO selectivity for both the sides is shown in Fig. 12. The selectivity to CO is higher compared to $H_2$ for the oxidation channel. However, for the reforming channel even though the CO selectivity is comparable to that of $H_2$ selectivity, at higher specific area, the selectivity is more towards $H_2$.

The coverages major surface adsorbed species at 0.1 ms and at steady state on the reforming bed and the oxidation bed are shown respectively in Figs. 13 and 14. The surface coverages of H atoms on Ni surface at 0.1ms and steady state are shown respectively in Fig. 13(a) and Fig. 13(b). The initial surface coverages of H atoms are higher compared to that at steady state. Figures 13(c) and 13(d) shows that CO is the major surface adsorbed species initially as well as at steady state. Free Ni surfaces at 0.1 ms as well as at steady state are shown respectively in Figs. 13(e) and 13(f).

In the case of oxidation the surface coverage of H atoms are insignificant at 0.1 ms (Fig. 14(a)) compared to that at steady state (Fig. 14(b)). CO is the major surface adsorbed species at initial time scales as well as at steady state which are displayed respectively in Fig. 14(c) and Fig. 14(d). Significant C deposition is observed downstream the reactor (Figs. 14(e) and 14(f)), which stems from unreacted $CH_4$ in the absence of a reactant. Near the reactor inlet, there is enough oxygen which converts $CH_4$ into products and therefore the C deposition is minimal near the inlet. Figs. 14(g) and 14(h) respectively

shows the free Rh surfaces at 0.1ms and at steady state. Due to C coverage downstream the reactor Rh surfaces are not freely available for adsorption.

Finally a comparison with thermodynamic equilibrium predictions can ensure that the calculations performed do not violate the underlying physics. For comparison with equilibrium predictions, we carry out isothermal calculations. The inlet conditions are same as those used for parameter study. The bed thickness on both sides is fixed at 50μm and the specific area is fixed at $35 \times 10^4 \text{m}^{-1}$ for the oxidation side and $50 \times 10^4 \text{m}^{-1}$ for the reforming side. Figs. 15 and 16 shows the $CH_4$ conversion respectively on the oxidation side and the reforming side in comparison with equilibrium predictions as a function of temperature. In both cases the kinetic predictions are within the limit set by equilibrium.

## 4. Conclusions

We have presented a quasi two dimensional pseudo transient numerical model for a catalytic plate reactor. The viability of catalytic plate reactor as on-board reformer is studied. The problems associated with $H_2O/CO_2$ management for on-board reforming can be mitigated by recycling the anode stream with the heat released from the oxidation reactions proceeding in the parallel channel of CPR. The system studied exhibits excellent heat management by supplying the necessary heat requirement of the endothermic reforming reactions.

## References

Baldea, M., Daoutidis, P., 2007. Dynamics and control of autothermal reactors for the production of hydrogen. Chem. Eng. Sci. 62, 3218–3230.

Bharadwaj, S. S., Schmidt, L. D., 1995. Catalytic partial oxidation of natural gas to syngas. Fuel Process. Technol. 42, 109–127.

Clarke, S. H., Dicks, A. L., Pointon, K., Smith, T. A., Swann, A., 1997. Catalytic aspects of steam reforming of hydrocarbons in internal reforming fuel cells. Catalysis Today 38, 411–423.

de Smet, C. R. H., 2000. Partial oxidation of methane to synthesis gas: Reaction kinetics and reactor modelling. Ph.D. thesis, Technical University of Eindhoven.

Deshmukh, S. R., Vlachos, D. G., 2005. Cfd simulations of coupled, countercurrent combustor/reformer microdevices for hydrogen production. Ind. Eng. Chem. Res. 44, 4982–4992.

Deuflhardt, P., Hairer, E., Zugk, J., 1987. One step and extrapolation methods for differential-algebraic systems. Numerische Mathematik 51, 501–516.

Hayes, R. E., Kolaczkowski, S. T., 1997. Introduction to catalytic combustion. Gordon and Breach Science Publishers, Amsterdam.

IANGV, 2010. Natural gas vehicle statistics. http://www.iangv.org/tools-resources/statistics.html.

Janardhanan, V. M., Deutschmann, O., 2006. Cfd analysis of solid oxide fuel cell with internal reforming: coupled interaction of transport, heterogeneous catalysis and electrochemical processes. J. Power Sources 162, 1192–1202.

Janardhanan, V. M., Heuveline, V., Deutschmann, O., 2007. Performance analysis of a sofc under direct internal reforming conditions. J. Power Sources 172, 296–307.

Kim, G. Y., Mayor, J. R., Ni, J., 2005. Parametric study of microreactor design for water gas shift reactor using an integrated reaction and heat exchanger model. Chem. Eng. J 110, 1–10.

Kiwi-Minsker, L., Renken, A., 2005. Microstructured reactors for catalytic reactions. Catal. Today 130, 2–1.

Kolb, G., Hessel, V., 2004. Micro-structured reactors for gas phase reactions. Chem. Eng. J 98, 1–38.

Lindermeir, A., Kah, S., kavurucu, S., Mühlner, M., 2007. On-board diesel fuel processing for an sofc-apu technical challenges for catalysis and reactor design. Appl. Catal., B 70, 488–497.

Monzón, A., Latorre, N., Ubieto, T., Royo, C., Romeo, E., Villacampa, J. I., Dussault, L., Dupin, J. C., Guimon, C., Montioux, M., 2006. Improvement of activity and stability of ni-mg-al catalysts by cu addition during hydrogen production by catalytic decomposition of methane. Catal. Today 116, 264–270.

Schädel, B., Duisberg, M., Deutschmann, O., 2009. Steam-reforming of methane, ethane, propane, butane and natural gas over a rhodium-based catalyst. Catal. Today 142, 42–51.

Schwiedernoch, R., Tischer, S., Correa, C., Deutschmann, O., 2003. Experimental and numerical study on the transient behaviour of partial oxidation of mathane in a catalytic monolith. Chem. Eng. Sci. 58, 633–642.

Stefanidis, G. D., Vlachos, D. G., 2008. Millisecond methane steam reforming via process and catalyst intensification. Chem Eng Technol 31, 1201–1209.

Stefanidis, G. D., Vlachos, D. G., Kaisare, N. S., Maestri, M., 2009. Methane steam reforming at microscales: Operation strategies for variable power output at millisecond contact times. AIChE J. 55, 180–191.

Vlachos, D. G., Caratzoulas, S., 2010. The role of catalysis and reaction engineering in overcoming the energy and the environmental crisis. Chem. Eng. Sci. 65, 18–29.

Xu, J., Froment, G. F., 1989a. Methane steam reforming ii: Diffusional limitaions and reactor simulation. AIChE J. 35, 97–103.

Xu, J., Froment, G. F., 1989b. Methane stean reforming, methanation and water-gas shift: I intrinsic kinetics. AIChE J. 35, 88–95.

Zafir, M., Gavriilidis, A., 2004. Influence of flow arrangement in catalytic plate reactors for mehtane steam reformig. Chem. Eng. Res. Des. 82, 252–258.

Zanfir, M., Gavriilidis, A., 2003. Catalytic combustion assisted methane steam reforming in a catalytic plate reactor. Chem. Eng. Sci. 58, 3947–3960.

Zhu, H., Kee, R. J., Janardhanan, V. M., Deutschmann, O., Goodwin, D. G., 2005. Modeling elementary heterogeneous chemistry and electrochemistry in solid oxide fuel cells. J. Electrochem. Soc. 152, A2427–A2440.

## Notations

| | |
|---|---|
| $A_i$ | Pre exponential factor |
| $A_s$ | Specific catalyst area (m$^{-1}$) |
| $A_{s,o}$ | Specific catalyst area for oxidation bed (m$^{-1}$) |
| $A_{s,r}$ | Specific catalyst area for reforming bed (m$^{-1}$) |
| $B_g$ | Permeability (m$^2$) |
| $c_p$ | Specific heat (J/kg K) |
| $D_h$ | Hydraulic diameter of the flow channel (m) |
| $d_p$ | Particle diameter (m) |
| $\mathcal{D}_{kl}^{DGM}$ | Matrix of dusty gas model diffusion coefficients (m$^2$ s$^{-1}$) |
| $\mathcal{D}_{l,Kn}^e$ | Effective Knudsen diffusion coefficient of species $l$ (m$^2$ s$^{-1}$) |
| $\mathcal{D}_{k,m}$ | Diffusion coefficient of species $k$ in the mixture (m$^2$ s$^{-1}$) |
| $\mathcal{D}_k^e$ | Effective diffusion coefficient of species $k$ in the porous me |
| $\mathcal{D}_{kl}^e$ | Effective binary diffusion coefficient of species $k$ in the por |
| $\bar{\mathcal{D}}_k$ | Diffusion coefficient of species $k$ in the porous media (m$^2$ s |
| $E_{ai}$ | Activation energy for $i$th reaction (J mol$^{-1}$) |
| $D_h$ | Hydraulic diameter (m) |
| $d_p$ | Pore diameter (m) |
| Gz | Graetz number |
| $H$ | Specific enthalpy of the mixture (J kg$^{-1}$ ) |
| $h$ | Heat transfer coefficient (J m$^{-2}$ s$^{-1}$ K$^{-1}$) |
| $h_k$ | Molar enthalpy of species $k$ (J mol$^{-1}$) |
| $J_k$ | Molar flux of species $k$ ( mol m$^{-2}$ s$^{-1}$) |
| $K_g$ | Number of gasphase species |
| $K_s$ | Number of surface species |

| $k_{fi}$ | Forward reaction rate constant |
| --- | --- |
| $L$ | Bed thickness (m) |
| $\dot{m}$ | mass flow rate (kg m$^{-2}$s$^{-1}$) |
| $\dot{n}$ | molar flow rate (mol m$^{-2}$s$^{-1}$) |
| Nu | Nusselt number |
| $p$ | Pressure (Pa) |
| Pr | Prandtl number |
| R | Recycle ratio |
| $R$ | Universal gas constant (J mol$^{-1}$ K$^{-1}$) |
| Re | Reynolds number |
| $\dot{s}_k$ | surface molar production rate of species $k$ (mol m$^{-2}$s$^{-1}$) |
| $T$ | Fluid temperature (K) |
| $T_s$ | Solid temperature (K) |
| $u$ | Average velocity (ms$^{-1}$ ) |
| $W_k$ | Molecular weight of species $k$ (kg mol$^{-1}$) |
| $\bar{W}$ | Average molecular weight of the mixture (kg mol$^{-1}$) |
| $[X_l]$ | Concentration of species $l$ |
| $X_k$ | Mole fraction of species $k$ |
| $Y_k$ | Mass fraction of species $k$ |
| $y$ | Y coordinate (m) |
| $z$ | Axial coordinate (m) |
| $\beta_i$ | Temperature exponent for modified Arrhenius expression |
| $\delta_{kl}$ | Kronecker delta |
| $\epsilon$ | porosity |
| $\epsilon_{ki}$ | Coverage dependent activation energy for species $k$ in reaction $i$ |
| $\theta_k$ | Surface coverage of species $k$ |
| $\lambda$ | Thermal conductivity (J m$^{-1}$ s$^{-1}$ K$^{-1}$) |
| $\mu$ | Viscosity (Kg m$^{-1}$ s$^{-1}$) |
| $\rho$ | Density (kg m$^{-3}$ ) |
| $\tau$ | Tortuosity |
| $\dot{\omega}_k$ | Gas-phase molar production rate of species $k$ (mol m$^{-3}$s$^{-1}$) |
| $\Gamma$ | Site density (mol m$^{-2}$) |

Table 1: Inlet gas compositions and geometric parameters used for calculations

| Gas phase | Reforming side | Combustion side | Geometry | Reforming side | Combustion side |
|---|---|---|---|---|---|
| ***Inlet conditions*** | | | ***Flow channel*** | | |
| Composition %(vol) | - | 30.0% $CH_4$ | Channel length (cm) | 5 | 5 |
| | - | 14.7% $O_2$ | Channel height (mm) | 1 | 1 |
| | - | 55.3% $N_2$ | ***Catalytic bed*** | | |
| Velocity (m s$^{-1}$) | - | 0.4 | thickness (μm) | 10-100 | 50 |
| Temperature (K) | 923.15 | 923.15 | Porosity | 40% | 40% |
| Pressure (atm) | 1 | 1 | Tortuosity | 4.0 | 4.0 |
| | | | Pore diameter (nm) | 1 | 1 |
| | | | Particle diameter (μm) | 1 | 1 |
| | | | Specific area $\times 10^{-5}$ (m$^{-1}$) | 0.5-15 | 3.5 |
| ***Solid wall parameters*** | | | Thermal diffusivity $\times 10^6$ (m$^2$ s$^{-1}$) | 3.4 | 3.4 |
| Thickness (mm) | 1 | | | | |
| Thermal diffusivity $\times 10^6$ (m$^2$ s$^{-1}$) | 45 | | | | |

The compositions and velocity at the reforming channel inlet is decided by the recycle ratio used. For parameter study the inlet compositions at the reforming channel are fixed as 13.6% $CH_4$, 40.8% $H_2O$, 20.4% $CO_2$ and 25.2% $N_2$ entering at a velocity of 0.2 m/s and 923.15 K.
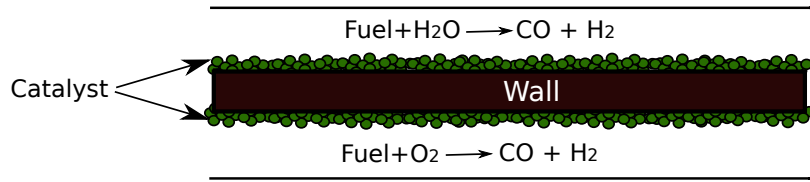
**Figure Captions**

1. Schematic representation of a catalytic plate reactor. Fuel combustion takes place in the bottom channel and reforming takes place in the top channel.
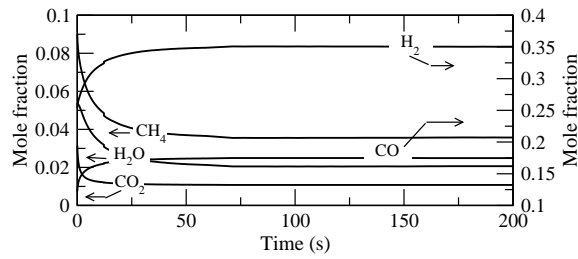
2. Species mole fractions at the exit of the oxidation channel. The inlet conditions for this case are given in Table 1. $A_s$=35×10$^4$ m$^{-1}$, $L$ = 50μm, $u$=0.4m s$^{-1}$ and $T$=923.15 K.
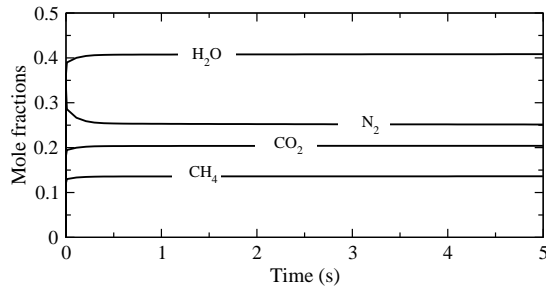
3. Species mole fractions at the inlet of reforming channel. 20% of the anode stream is recycled. $A_{s,o}$=35×10$^4$ m$^{-1}$, $A_{s,r}$=50×10$^4$ m$^{-1}$, $L$ = 50μm and $T$=923.15 K.
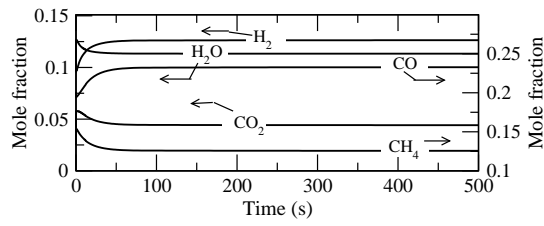
4. Species mole fractions at the exit of reforming channel. 20% of the anode stream is recycled. $A_{s,o}$=35×10$^4$ m$^{-1}$, $A_{s,r}$=50×10$^4$ m$^{-1}$, $L$ = 50μm and $T$=923.15 K.
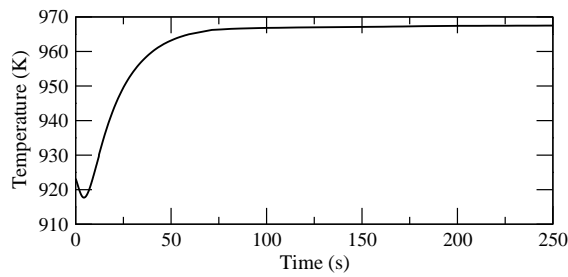
5. Temperature of the reforming and oxidation channel at the reactor exit as a function of time. Since they overlap only one is shown.

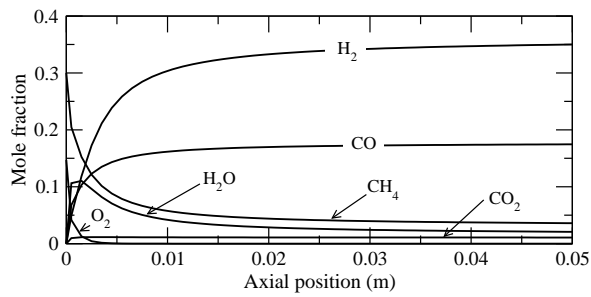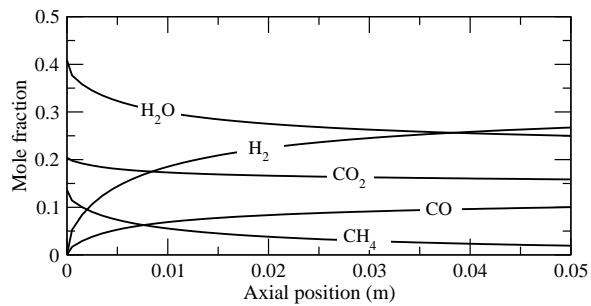6. Species profiles in the oxidation channel as a function of reactor position at steady state. $A_s$=35×10$^4$ m$^{-1}$, $L$ = 50μm and $T$=923.15 K

7. Species profiles in the reforming channel as a function of reactor position at steady state. $A_s$=50×10$^4$ m$^{-1}$, $L$ = 50μm and $T$=923.15 K
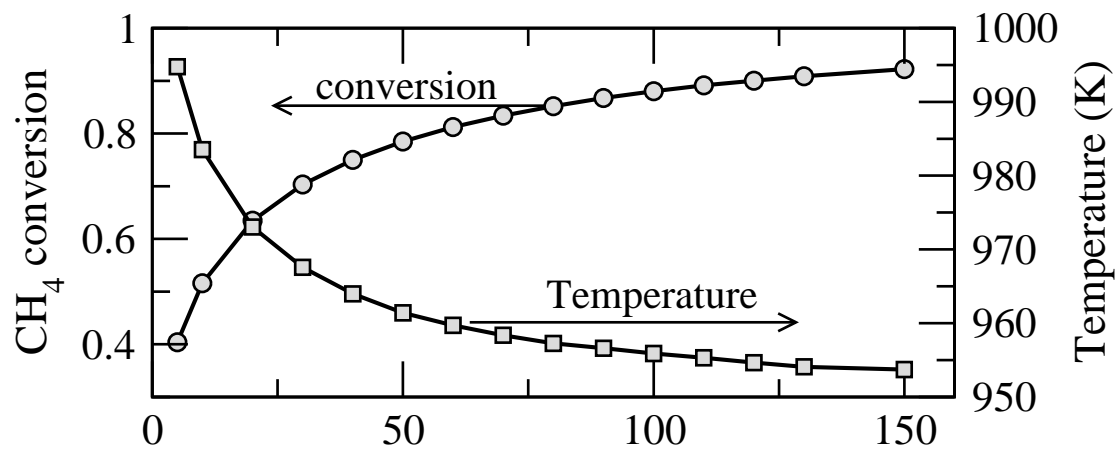
8. Methane conversion in the reforming channel and the products exit temperature as a function of specific catalyst area. The specific area on the oxidation bed is kept constant at 35×10$^4$ m$^{-1}$. The inlet velocity for the reforming channel is 0.2 m s$^{-1}$ and the bed thickness is 50 μm
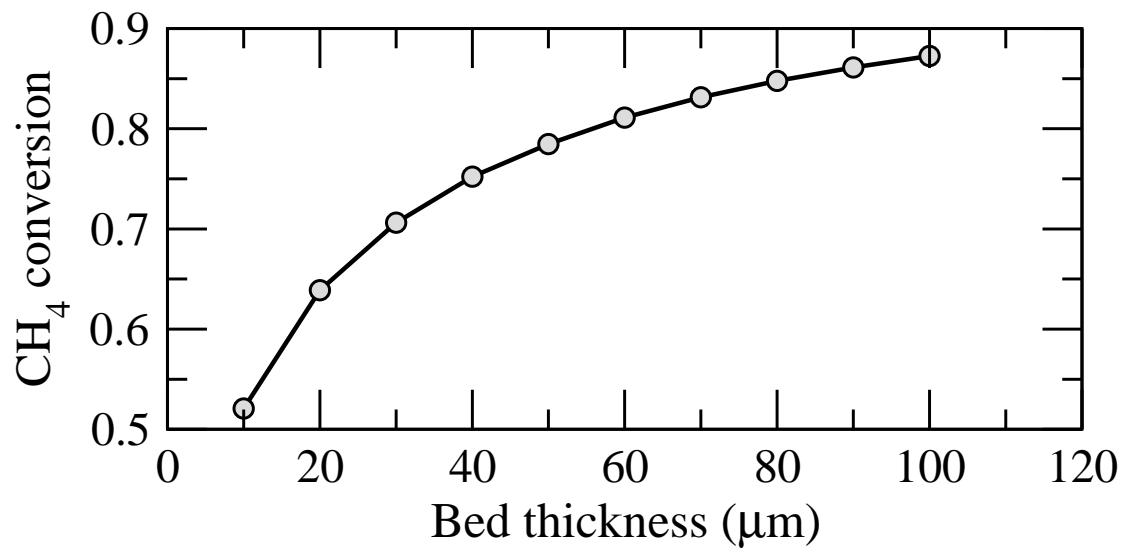
9. Methane conversion in the reforming channel as a function of bed thickness. The bed thickness of oxidation channel is kept constant at 50μm. Specific catalyst area for oxidation side is 35×10$^4$ and for reforming side is 50×10$^4$ m$^{-1}$. The inlet velocity for reforming channel is 0.2 m s$^{-1}$

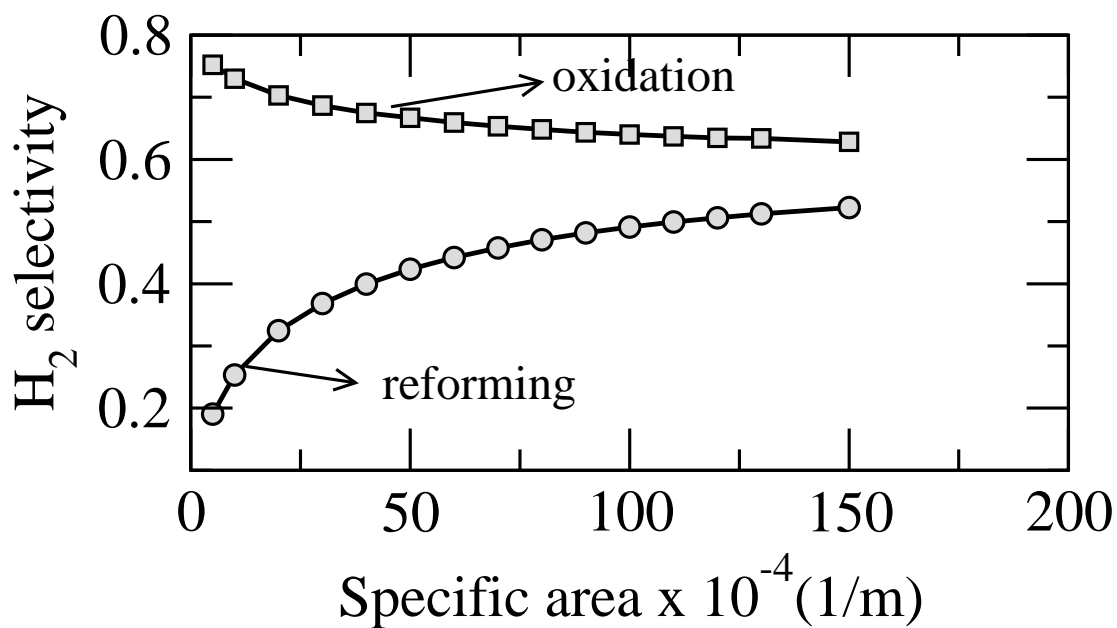10. H$_2$ selectivity a function of specific area. The inlet velocity for the reforming channel is 0.2 m s$^{-1}$ and the bed thickness is 50μm
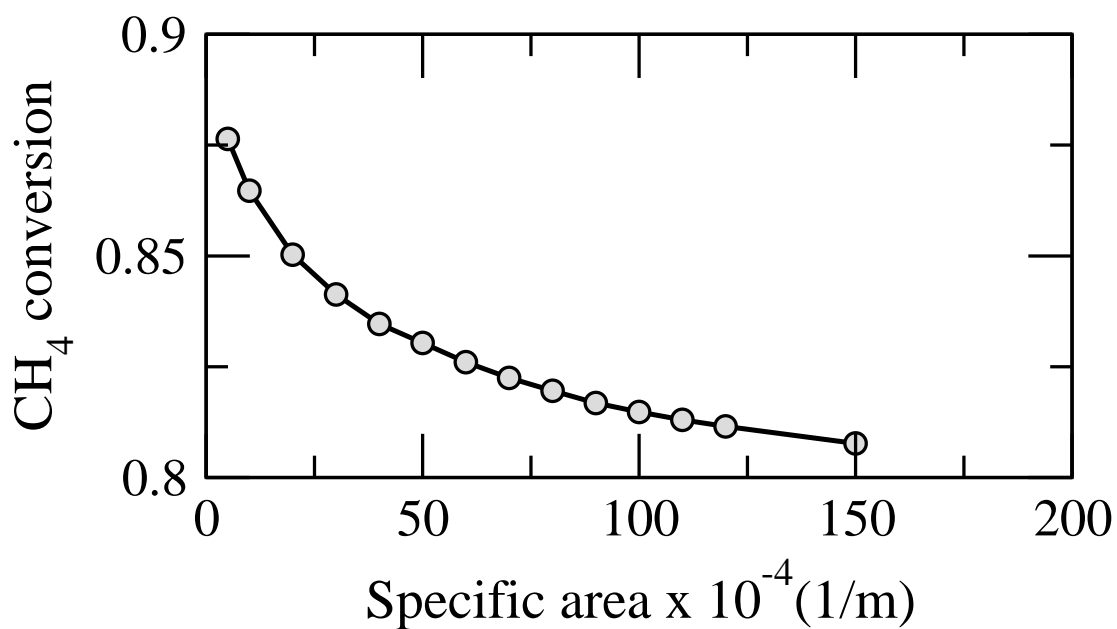
11. Methane conversion in the oxidation channel as a function of specific catalyst area on the reforming side. The specific area on the oxidation bed is kept constant at 35×10$^4$ m$^{-1}$. The inlet velocity for the reforming channel is 0.2 m s$^{-1}$ and both the bed thicknesses are 50 μm
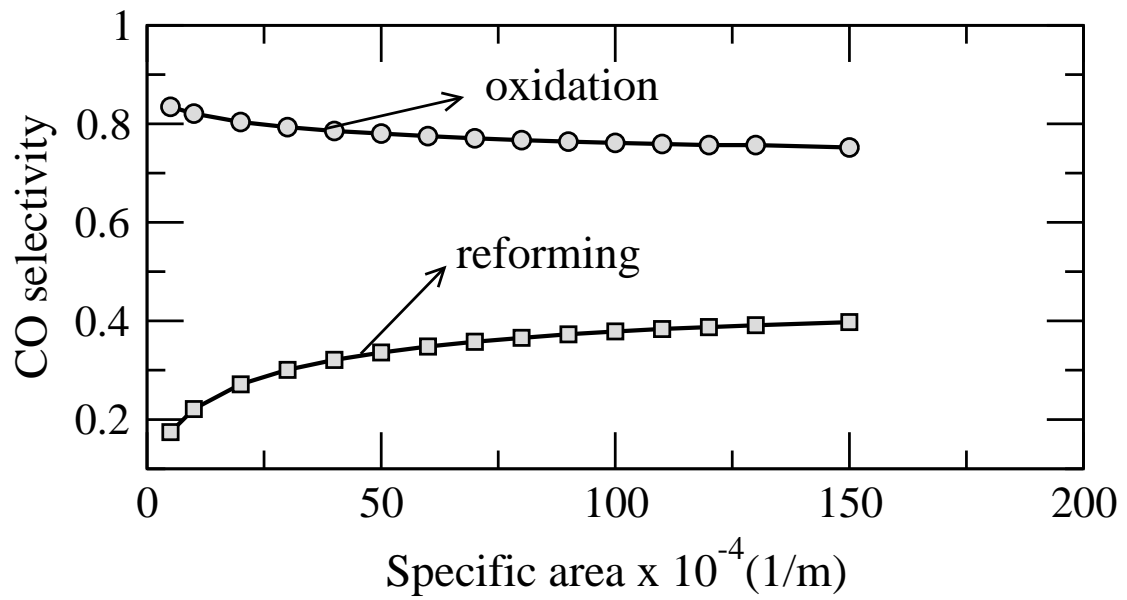
12. CO selectivity a function of specific area. The inlet velocity in the reforming channel is 0.2 m s$^{-1}$ and both the bed thicknesses are 50μm

13. Surface coverages of major surface adsorbed species and the free Ni surfaces on the reforming side at 0.1 ms and at steady state.

    (a) Surface coverage of H ad-atoms on the reforming bed at 0.1 ms.
    (b) Surface coverage of H ad-atoms on the reforming bed at steady state.
    (c) Surface coverage of CO on the reforming bed at 0.1 ms.
    (d) Surface coverage of CO on the reforming bed at steady state.
    (e) Free Ni surfaces on the reforming bed at 0.1 ms.
    (f) Free Ni surfaces on the reforming bed at steady state.

14. Surface coverages of major surface adsorbed species and the free Rh surfaces on the reforming side at 0.1 ms and at steady state.

    (a) Surface coverage of H ad-atoms on the oxidation bed at 0.1 ms.
    (b) Surface coverage of H ad-atoms on the oxidation bed at steady state.
    (c) Surface coverage of CO on the oxidation bed at 0.1 ms.
    (d) Surface coverage of CO on the oxidation bed at steady state.
    (e) Surface coverage of C on the oxidation bed at 0.1 ms.
    (f) Surface coverage of C on the oxidation bed at steady state.
    (g) Free Rh surfaces on the oxidation bed at 0.1 ms.
    (h) Free Rh surfaces on the oxidation bed at steady state.

15. Comparison of CH$_4$ conversion on the oxidation side with equilibrium predictions

16. Comparison of CH$_4$ conversion on the reforming side with equilibrium predictions

Figure 1: Schematic representation of a catalytic plate reactor. Fuel combustion takes place in the bottom channel and reforming takes place in the top channel.



Figure 2: Species mole fractions at the exit of the oxidation channel. The inlet conditions for this case are given in Table 1. $A_s$=35×10$^4$ m$^{-1}$, $L$ = 50μm, $u$=0.4m s$^{-1}$ and $T$=923.15 K



Figure 3: Species mole fractions at the inlet of reforming channel. 20% of the anode stream is recycled. $A_{s,o}$=35×10$^4$ m$^{-1}$, $A_{s,r}$=50×10$^4$ m$^{-1}$, $L$ = 50μm and $T$=923.15 K.

Figure 4: Species mole fractions at the exit of reforming channel. 20% of the anode stream is recycled. $A_{s,o}$=35×10$^4$ m$^{-1}$, $A_{s,r}$=50×10$^4$ m$^{-1}$, $L$ = 50μm and $T$=923.15 K



Figure 5: Temperature of the reforming and oxidation channel at the reactor exit as a function of time. Since they overlap only one is shown.



Figure 6: Species profiles in the oxidation channel as a function of reactor position at steady state. $A_s$=35×10$^4$ m$^{-1}$, $L$ = 50μm and $T$=923.15 K



Figure 7: Species profiles in the reforming channel as a function of reactor position at steady state. $A_s$=50×10$^4$ m$^{-1}$, $L$ = 50μm and $T$=923.15 K

10

Figure 8: Methane conversion in the reforming channel and the products exit temperature as a function of specific catalyst area. The specific area on the oxidation bed is kept constant at $35\times10^4$ m$^{-1}$. The inlet velocity for the reforming channel is 0.2 m s$^{-1}$ and the bed thickness is 50 μm



Figure 9: Methane conversion in the reforming channel as a function of bed thickness. The bed thickness of oxidation channel is kept constant at 50μm. Specific catalyst area for oxidation side is $35\times10^4$ and for reforming side is $50\times10^4$ m$^{-1}$. The inlet velocity for reforming channel is 0.2 m s$^{-1}$

Figure 10: H$_2$ selectivity a function of specific area. The inlet velocity for the reforming channel is 0.2 m s$^{-1}$ and the bed thickness is 50μm



Figure 11: Methane conversion in the oxidation channel as a function of specific catalyst area on the reforming side. The specific area on the oxidation bed is kept constant at 35×10$^4$ m$^{-1}$. The inlet velocity for the reforming channel is 0.2 m s$^{-1}$ and both the bed thickness's are 50 μm

Figure 12: CO selectivity a function of specific area. The inlet velocity in the reforming channel is 0.2 m s$^{-1}$ and both the bed thickness's are 50μm
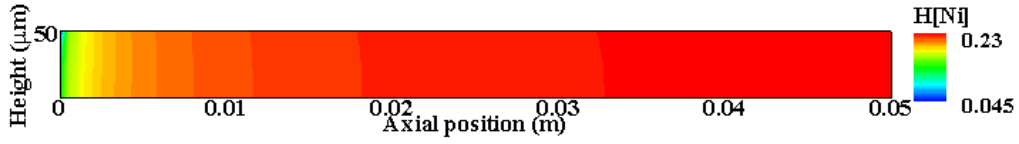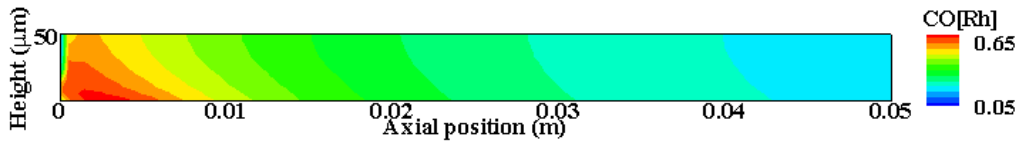
(a) Surface coverage of H ad-atoms on the reforming bed at 0.1 ms.
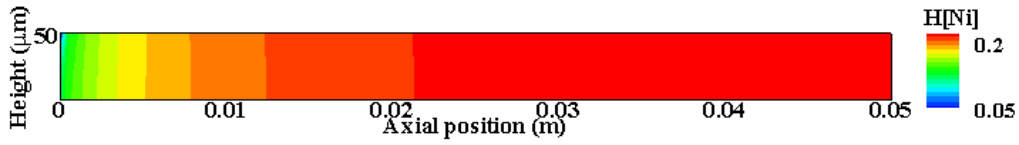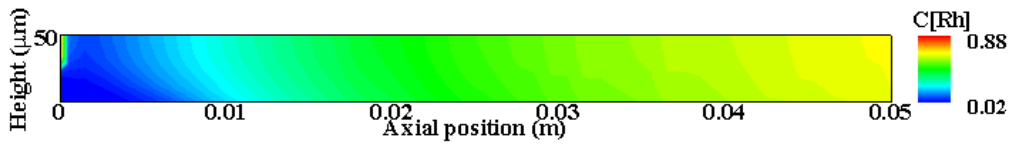


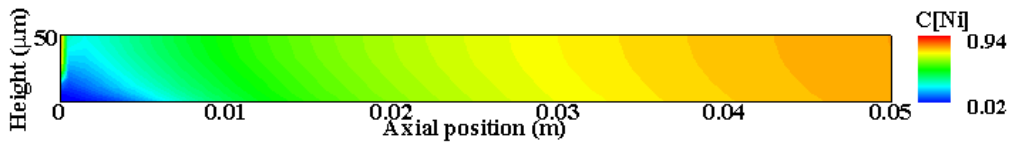(b) Surface coverage of H ad-atoms on the reforming bed at steady state.
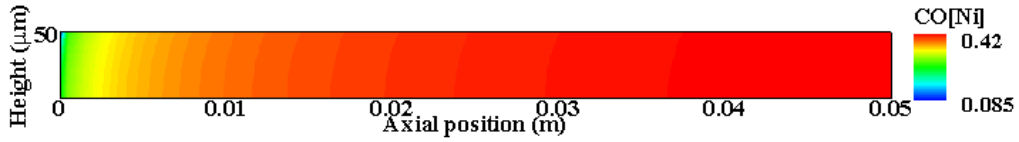


(c) Surface coverage of CO on the reforming bed at 0.1 ms.
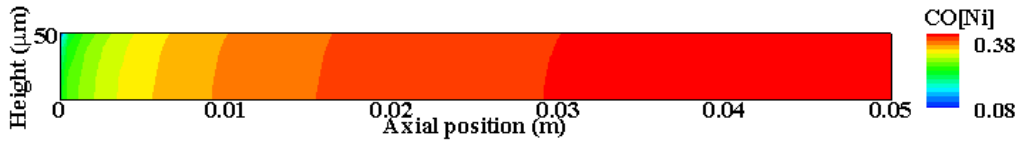


(d) Surface coverage of CO on the reforming bed at steady state.
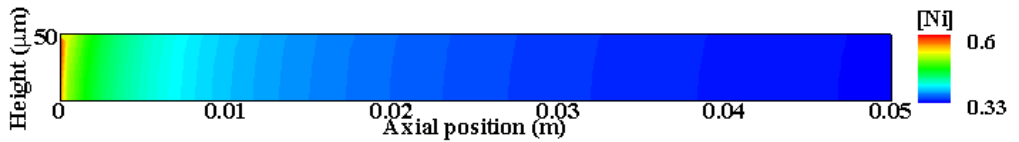


(e) Free Ni surfaces on the reforming bed at 0.1 ms.
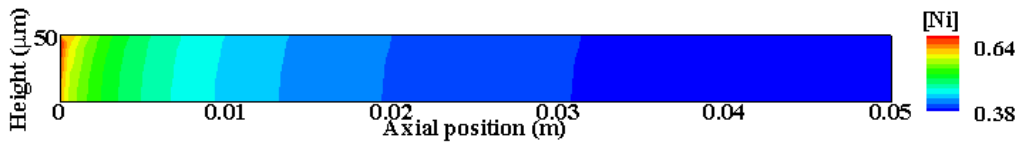


(f) Free Ni surfaces on the reforming bed at steady state.

Figure 13: Surface coverages of major surface adsorbed species and the free Ni surfaces on the reforming side at 0.1 ms and at steady state.

(a) Surface coverage of H ad-atoms on the oxidation bed at 0.1 ms.



(b) Surface coverage of H ad-atoms on the oxidation bed at steady state.
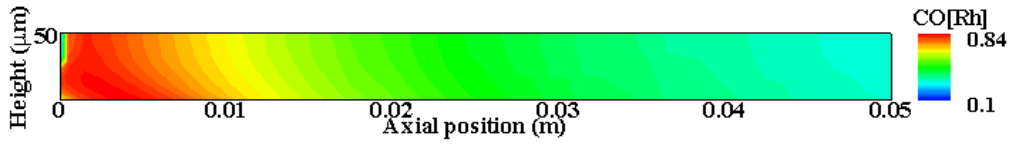


(c) Surface coverage of CO on the oxidation bed at 0.1 ms.
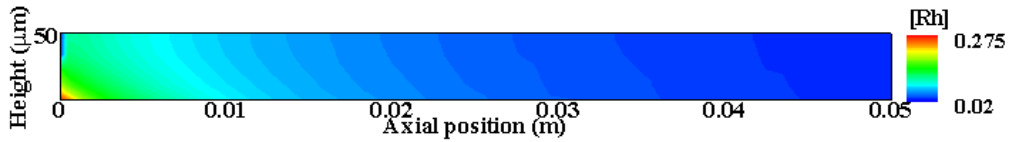


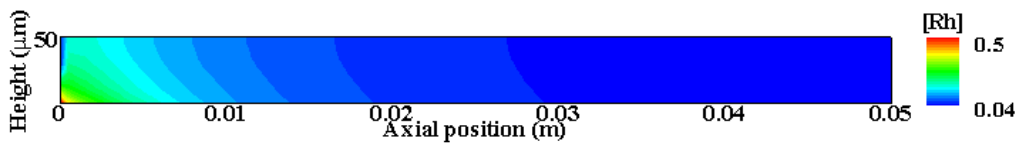(d) Surface coverage of CO on the oxidation bed at steady state.



(e) Surface coverage of C on the oxidation bed at 0.1 ms.



(f) Surface coverage of C on the oxidation bed at steady state.



(g) Free Rh surfaces on the oxidation bed at 0.1 ms.



(h) Free Rh surfaces on the oxidation bed at steady state.

Figure 14: Surface coverages of major surface adsorbed species and the free Rh surfaces on the oxidation side at 0.1 ms and at steady state.
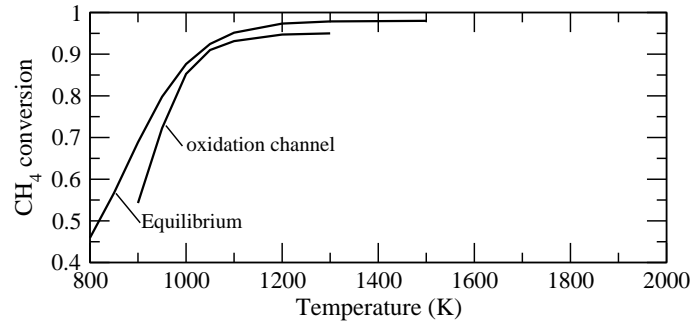
Figure 15: Comparison of CH$_4$ conversion on the oxidation side with equilibrium predictions
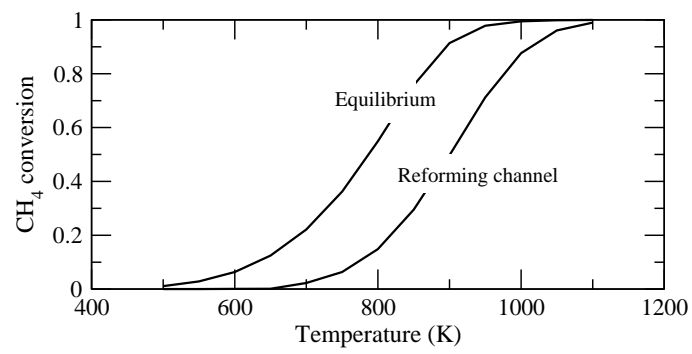


Figure 16: Comparison of CH$_4$ conversion on the reforming side with equilibrium predictions